PAPER

Check for updates

Construction of bimetallic oxy-hydroxides based on Ni(OH)₂ nanosheets for sensitive non-enzymatic glucose detection *via* electrochemical oxidation and incorporation†

Weiji Dai, [ID] *[a] Bing Wu,[a] Fan Zhang,[a] Yuxi Huang,[a] Cuijiao Zhao,[a] Yudong Zhang,[a] Can Cui,[a] Jing Guo[b] and Saifang Huang*[a]

Due to their ease of synthesis and large specific surface area, $Ni(OH)_2$ nanosheets have emerged as promising electrochemical sensing materials, attracting significant attention in recent years. Herein, a series of oxy-hydroxides based on $Ni(OH)_2$ nanosheets, including $NiO_x/Ni(OH)_2$@NF and $(MNi)O_x/Ni(OH)_2$@NF (M = Co, Fe, or Cr), are successfully synthesized *via* the electrochemical oxidation and incorporation strategies. Electrochemical tests demonstrate that these $Ni(OH)_2$-based oxy-hydroxides exhibit excellent electrochemical oxidation activity for glucose in alkaline electrolyte. Among these, $(CoNi)O_x/Ni(OH)_2$@NF displays higher sensitivity of 3590.3 $\mu A\ mM^{-1}\ cm^{-2}$ across a broad linear range of 10 μM to 1.14 mM, with a rapid current response time of less than 4 s. The superior sensing performances of $(CoNi)O_x/Ni(OH)_2$@NF are attributed to the formation of abundant Ni^{3+} species and reactive-O atoms due to the electrochemical oxidation, and the synergistic effects of Co/Ni active sites resulting from the electrochemical incorporation process. In addition, the $(CoNi)O_x/Ni(OH)_2$@NF demonstrates good stability and reproducibility for glucose sensing. This work fully leverages the significance of surface reconstruction of $Ni(OH)_2$, providing new insights for the application of transition metal-based oxy-hydroxide materials in bio-sensing.

[a]School of Materials Science and Engineering, Jiangsu University of Science and Technology, Zhenjiang 212003, China. E-mail: daiweiji@just.edu.cn, s.huang@just.edu.cn

[b]School of Resources and Materials, Northeastern University at Qinhuangdao, Qinhuangdao 066004, China

†Electronic supplementary information (ESI) available. See DOI: https://doi.org/10.1039/d4nr04342a

Weiji Dai received his PhD degree from Southeast University in 2021. He is currently a lecturer at the School of Materials Science and Engineering, Jiangsu University of Science and Technology. His research interests are mainly focused on the synthesis, functionalization, catalytic mechanism, and applications of metastable materials (e.g. amorphous and high-entropy materials).

Weiji Dai

1. Introduction

The concentration of glucose in blood is a significant index to reflect the health condition of the human body.[1,2] As is known to all, low glucose concentration will make people feel weak and even go unconscious, while a long-term high concentration of glucose in the blood will increase the risk of human obesity, diabetes and other chronic diseases.[3] Thus, developing accurate and efficient glucose sensors is of great significance for human health monitoring. In addition, glucose sensors also play an important role in the food industry.[4,5] Typically, glucose detection can be achieved through two methods: enzymatic sensing and non-enzymatic sensing.[6–8] The enzymatic sensors exhibit high selectivity and sensitivity for glucose detection; however, their activity can be easily affected by the temperature and pH of the environment.[9,10] Compared with enzymatic sensors, the recently developed non-enzymatic sensors not only have high sensitivity, outstanding stability, and fast response speed for glucose detection, but also show good stability to the detection environment.[11,12]

Currently, a variety of materials have been investigated as non-enzymatic glucose sensors, such as precious metals rep-

resented by Pt and Au.[13,14] Pt is well-known as a state-of-the-art electrocatalyst for the hydrogen evolution reaction.[15,16] Here, Pt also shows excellent catalytic ability for glucose oxidation; however, it has low anti-interference ability since it can be easily affected by uric acid in the blood.[17] Au has a strong selectivity and a low oxidation potential for glucose detection, but its high-cost has limited its commercial application.[18,19] Fortunately, non-precious transition metal-based materials represented by Co, Ni, Cu, and their compounds have been intensively investigated as promising candidates for glucose sensing.[20–22] Benefiting from the well-designed nanostructure, researchers have obtained a series of transition metal-based alloys, oxides, and hydroxides with a large specific surface area and abundant active sites for non-enzymatic glucose detection.[23–25] It is worth mentioning that transition metal-based oxy-hydroxides are considered to be the true active materials for glucose sensing according to the widely accepted catalytic mechanism of glucose oxidation,[26,27] and thus the M^{2+}/M^{3+} couples are identified as the active sites. In this regard, designing an active surface with abundant M^{2+}/M^{3+} couples is a promising strategy to enhance the sensing ability for glucose.[28,29] Moreover, introducing extra catalytic sites to achieve synergistic effects can further contribute to the catalytic performance of glucose oxidation.[30,31]

Based on the above considerations, bimetallic oxy-hydroxides based on $Ni(OH)_2$ nanosheets ($(CoNi)O_x/Ni(OH)_2@NF$) were designed and prepared as high performance non-enzymatic sensors for glucose. In this work, electrochemical oxidation was conducted on $Ni(OH)_2$ nanosheets to prepare an active surface with abundant Ni^{3+} species (NiOOH) and reactive-O atoms. Subsequently, Co^{2+} ions were incorporated onto the active surface *via* electrochemical deposition, thus forming a bimetallic oxy-hydroxide electrocatalyst ($(CoNi)O_x/Ni(OH)_2@NF$). XPS results revealed that highly active Co^{4+} species were obtained on the surface of $(CoNi)O_x/Ni(OH)_2@NF$. With the help of abundant reactive-O atoms, the Co^{4+} species can accelerate the transformation of Ni^{2+} to Ni^{3+} species (NiOOH), which has been recognized as one of the most active materials for oxidizing glucose to gluconolactone. Thanks to the synergistic effects of the Co/Ni bimetallic sites, the $(CoNi)O_x/Ni(OH)_2@NF$ exhibited good glucose sensing performance, including a high sensitivity of 3590.3 μA mM^{-1} cm^{-2} in a linear range of 10 μM to 1.14 mM, and a fast response time of less than 4 s. Meanwhile, the obtained $(CoNi)O_x/Ni(OH)_2@NF$ had favorable selectivity and stability in glucose sensing.

2. Experimental

2.1. Chemicals

Nickel nitrate ($Ni(NO_3)_2\cdot 6H_2O$, ≥98%), urea ($CO(NH_2)_2$, ≥99%), ammonium fluoride (NH_4F, ≥96%), potassium hydroxide (KOH, ≥85%), iron nitrate ($Fe(NO_3)_3\cdot 9H_2O$, ≥98%), cobalt nitrate ($Co(NO_3)_2\cdot 6H_2O$, ≥99%), chromium nitrate ($Cr(NO_3)_3\cdot 9H_2O$, ≥99%), sodium hydroxide (NaOH, ≥99.9%),

glucose ($C_6H_{12}O_6$, ≥99.5%), ascorbic acid (AA, ≥99%), uric acid (UA, ≥99%), dopamine (DA, ≥98%), sodium chloride (NaCl, ≥99.8%), and fructose (≥99%) were purchased from Aladdin Chemical Co. Ltd, China. All chemicals mentioned above were used as supplied, without any further treatment. Nickel foam (NF) used as the substrate for the catalysts was provided by Suzhou Wingrise Energy Technology Co. Ltd, China. In order to remove the oxides on the surface, the tailored NF with a working area of 1 cm^2 was cleaned sequentially with 2 M HCl solution, anhydrous ethanol, and deionized water for 5 min each. Finally, the cleaned NF was dried in an oven at 60 °C for 1 h.
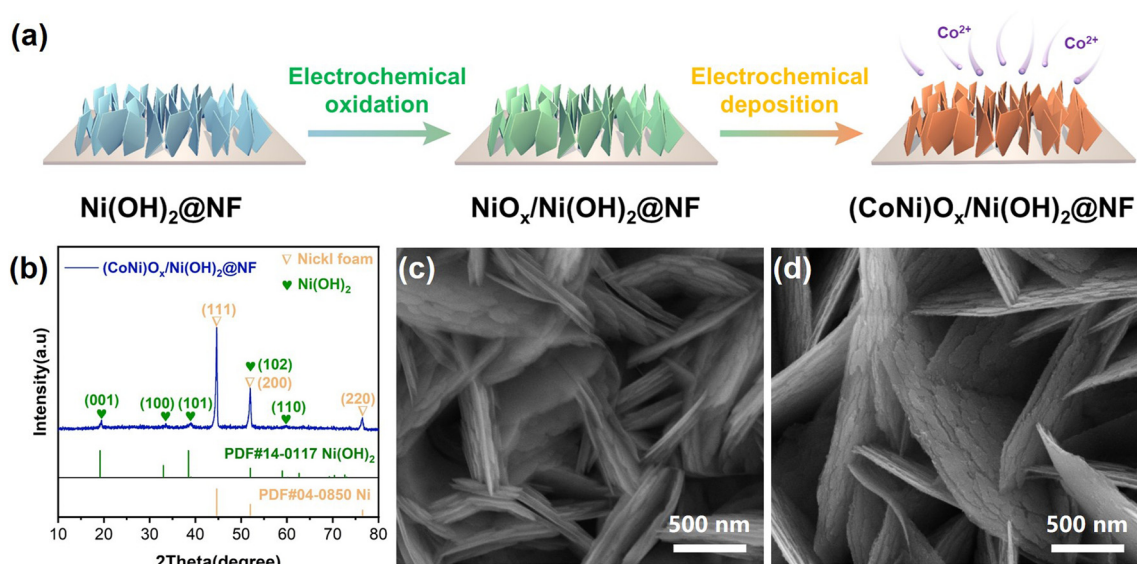
2.2. Preparation of $Ni(OH)_2@NF$

The $Ni(OH)_2$ nanosheets were synthesized through a typical hydrothermal method with NF as the substrate. Initially, a homogeneous solution was prepared with NH_4F (0.074 g), $Ni(NO_3)_2\cdot 6H_2O$ (0.291 g), and $CO(NH_2)_2$ (0.15 g) dissolved in deionized water (30 mL). Afterwards, the obtained solution was transferred into a Teflon-lined stainless-steel autoclave, along with two pieces of pre-treated NF. Subsequently, the sealed autoclave was heated to 120 °C in 1 h, and kept for 6 h. After naturally cooling to room temperature, the obtained $Ni(OH)_2@NF$ was further cleaned with deionized water and anhydrous ethanol, respectively. Finally, the $Ni(OH)_2@NF$ was dried in an oven at 60 °C for 1 h.

2.3. Preparation of $NiO_x/Ni(OH)_2@NF$

The $NiO_x/Ni(OH)_2@NF$ was prepared *via* electrochemical oxidation on $Ni(OH)_2@NF$ in 1 M KOH solution. As reported in our previous work, a standard three-electrode system was employed with $Ni(OH)_2@NF$ as the working electrode, a Pt sheet as the counter electrode, and an Ag/AgCl electrode as the reference electrode.[32] The electrochemical oxidation was performed at a constant potential of 0.656 V (*vs.* Ag/AgCl), corresponding to an initial current density of 20 mA cm^{-2} for the oxygen evolution reaction (OER). As the current–time ($i–t$) curve shows in Fig. S1,† the OER current density obviously increased in the first 2 h, indicating that surface reconstruction occurred, and reached stability in the next 3 h. After the electrochemical oxidation, the $NiO_x/Ni(OH)_2@NF$ was washed with deionized water and anhydrous ethanol sequentially.

2.4. Preparation of $(CoNi)O_x/Ni(OH)_2@NF$, $(FeNi)O_x/Ni(OH)_2@NF$, and $(CrNi)O_x/Ni(OH)_2@NF$

The $(CoNi)O_x/Ni(OH)_2@NF$ was obtained *via* electrochemical incorporation of Co^{2+} ions onto the $NiO_x/Ni(OH)_2@NF$ as illustrated in Fig. 1a. Firstly, a homogeneous solution was prepared by dissolving 0.291 g of $Co(NO_3)_2\cdot 6H_2O$ in 50 mL of deionized water as the electrolyte for electrochemical incorporation. Secondly, cyclic voltammetry (CV) scanning was conducted on the $NiO_x/Ni(OH)_2@NF$ at a scan rate of 10 mV s^{-1} for 5 cycles, with the voltage ranging from −1.2 to 0.6 V (*vs.* Ag/AgCl). Finally, the obtained $(CoNi)O_x/Ni(OH)_2@NF$ was sequentially rinsed with deionized water and anhydrous ethanol.

Fig. 1 (a) Schematic illustration of the preparation process of bimetallic oxy-hydroxides on Ni(OH)$_2$ nanosheets. (b) XRD pattern of (CoNi)O$_x$/Ni(OH)$_2$@NF. SEM images: (c) NiO$_x$/Ni(OH)$_2$@NF, and (d) (CoNi)O$_x$/Ni(OH)$_2$@NF.

The preparation processes of (FeNi)O$_x$/Ni(OH)$_2$@NF and (CrNi)O$_x$/Ni(OH)$_2$@NF are similar to that of (CoNi)O$_x$/Ni(OH)$_2$@NF except for the electrolyte used for electrochemical incorporation. As for the preparation of (FeNi)O$_x$/Ni(OH)$_2$@NF, 0.4041 g Fe(NO$_3$)$_3$·9H$_2$O was dissolved in 50 mL of deionized water to obtain the electrolyte. Similarly, 0.4002 g Cr(NO$_3$)$_3$·9H$_2$O was dissolved in 50 mL of deionized water to obtain the electrolyte for the preparation of (CrNi)O$_x$/Ni(OH)$_2$@NF.

2.5. Material characterization

The phase composition and crystal structure were determined by X-ray diffraction (XRD) on a Bruker-D2 PHASER instrument (Bruker AXS) using Cu-Kα radiation (λ = 1.5418 Å). Specifically, the spectra were recorded over a 2θ range from 10 to 80° with a step size of 0.02° and a dwell time of 0.1 s per step, under operating conditions of 30 kV and 10 mA. The microstructure of the catalysts was examined using scanning electron microscopy (SEM) on a Quanta 250 FEG instrument (Thermo Fisher Scientific Inc.) and transmission electron microscopy (TEM) on a Tecnai G2 F30 S-TWIN (FEI). The surface composition, chemical state, and bonding configuration were assessed *via* X-ray photoelectron spectroscopy (XPS) using a Kratos-AXIS system, with the C 1 s peak at a binding energy of 284.8 eV used for spectral calibration.

2.6. Electrochemical measurements

All electrochemical experiments were performed using a CHI 660E electrochemical workstation with a standard three-electrode configuration. In this configuration, the Ag/AgCl electrode (saturated KCl) and the platinum sheet electrode were used as the reference electrode and counter electrode, respectively. A 0.1 M NaOH solution (100 mL) was employed as the

electrolyte for glucose detection measurements. The geometric area of the working electrode immersed in the electrolyte was 1 cm^2. The electrochemical performance of the glucose sensor was evaluated using CV scanning and chronoamperometry methods, where $\Delta I = I_{Response} - I_{Initial}$. CV scanning measurements were performed over a potential range of 0 to 0.8 V (*vs.* Ag/AgCl) at a scan rate of 10 mV s^{-1}, unless otherwise specified. During the chronoamperometry tests, the electrolyte was stirred at 200 rpm to facilitate convective transport. All tests were conducted under optimal conditions unless otherwise specified in the text.

3. Results and discussion

The crystal structure of the samples was characterized using the XRD technique. Fig. S2† displays the XRD results of Ni(OH)$_2$@NF and NiO$_x$/Ni(OH)$_2$@NF, showing that Ni(OH)$_2$ was successfully synthesized on the NF substrate *via* a one-step hydrothermal reaction, and Ni(OH)$_2$ still existed after the electrochemical oxidation process. In this case, the Ni(OH)$_2$ served as a base material for preparing the active surface of NiO$_x$, which was found with abundant reactive-O atoms and Ni^{3+} species formed due to the electrochemical oxidation process. The electrochemical oxidation of Ni(OH)$_2$@NF was conducted under a voltage of 0.656 V (*vs.* Ag/AgCl), which can deliver considerable current density of the OER. The derived OER intermediates, such as OH$_{ads}$, O$_{ads}$, OOH$_{ads}$, and O$_{2ads}$, were adsorbed on metallic sites resulting in the formation of M–OH, M–O, M–OOH and M–O$_2$. Among them, the O$_{ads}$ was regarded as the reactive-O atom, which can bond with one adsorbed OH$^-$ to form the OOH$_{ads}$.[32] As shown in Fig. S3,† the XPS spectra of Ni 2p and O 1s display that the contents of Ni^{3+} increased from 41.4% to 41.9%, and the contents of Ni–O

bonds increased from 32.9% to 40.5% for the NiO_x/$Ni(OH)_2$@NF. This indicates that more Ni^{3+} species and reactive-O atoms formed due to the electrochemical oxidation. After the electrochemical incorporation of Co^{2+} ions onto the reconstructed surface, the XRD spectra of $(CoNi)O_x$/$Ni(OH)_2$@NF showed similar diffraction peaks to those of NiO_x/$Ni(OH)_2$@NF. As shown in Fig. 1b, the diffraction peaks at 44.7°, 52.0°, and 76.4° correspond perfectly to the (111), (200), and (220) crystal planes of metallic Ni (PDF#04-0850), primarily attributed to the chosen NF substrate. Meanwhile, the diffraction peaks at 19.4°, 33.5°, 39.1°, 52.1°, and 59.8° correspond to the reflection planes of (001), (100), (101), (102), and (110), respectively, which are characteristic of the pure hexagonal phase of $Ni(OH)_2$ (PDF#14-0117). Therefore, the XRD analysis indicates that the $Ni(OH)_2$ was not completely reconstructed by the electrochemical oxidation and deposition. In Fig. 1c and d, the SEM images show a morphology of cross-grown nanosheets for both the NiO_x/$Ni(OH)_2$@NF and $(CoNi)O_x$/$Ni(OH)_2$@NF electrodes, which is consistent with the microstructure of $Ni(OH)_2$@NF (Fig. S4†). Therefore, the SEM results further confirm the XRD results that $Ni(OH)_2$ nanosheets were

not completely reconstructed by the electrochemical oxidation and deposition; thus, the $Ni(OH)_2$ nanosheets served as a template for further preparing the bimetallic oxy-hydroxides. It is worth mentioning that the sheet-like morphology of the $Ni(OH)_2$ template is believed to bring a larger surface area of the prepared electrodes, benefiting the exposure of catalytic sites.[33]

The surface reconstructed $Ni(OH)_2$ nanosheets were further investigated via TEM methods to show the changes that resulted from the electrochemical deposition. As shown in Fig. 2a, the TEM image of a $(CoNi)O_x$/$Ni(OH)_2$ nanosheet displays obvious differences between the rim and core of the nanosheet. Selected area electronic diffraction (SAED) was performed on the core area of the $(CoNi)O_x$/$Ni(OH)_2$ nanosheet, showing a clear crystal structure corresponding to the hexagonal phase of $Ni(OH)_2$. According to the SAED pattern in Fig. 2b, the marked diffraction points can well correspond to the (100) and (111) planes of $Ni(OH)_2$. Meanwhile, the high-resolution TEM (HRTEM) image of the core area of the $(CoNi)O_x$/$Ni(OH)_2$ nanosheet clearly displays an interplanar spacing of about 0.258 nm (Fig. 2c), confirming the (100) plane of
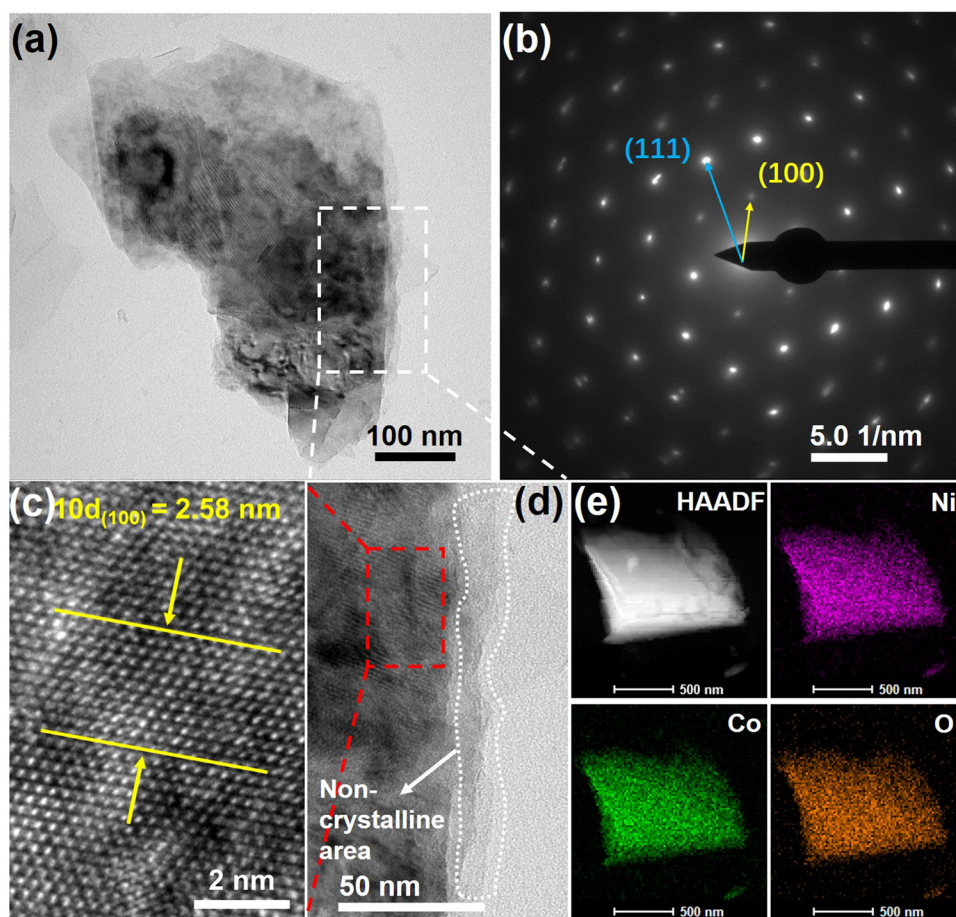
Fig. 2 (a) TEM image of $(CoNi)O_x$/$Ni(OH)_2$@NF. (b) SAED pattern of the core area of $(CoNi)O_x$/$Ni(OH)_2$@NF. (c) High-resolution TEM image of the core area of $(CoNi)O_x$/$Ni(OH)_2$@NF. (d) TEM image of the rim area of $(CoNi)O_x$/$Ni(OH)_2$@NF. (e) HAADF and elemental mappings of $(CoNi)O_x$/$Ni(OH)_2$@NF.

Ni(OH)$_2$. However, the TEM image in Fig. 2d reveals a non-crystalline characteristic for the rim area of the (CoNi)O$_x$/Ni(OH)$_2$ nanosheet as marked with the white dashed line, indicating that the surface of the Ni(OH)$_2$ nanosheet was reconstructed due to the electrochemical oxidation and deposition. The high angle annular dark field (HAADF) image and elemental mappings in Fig. 2e show that Co^{2+} ions were successfully incorporated onto the reconstructed surface of the NiO$_x$/Ni(OH)$_2$@NF, since the elements Co, Ni, and O were uniformly distributed across the whole nanosheet. In addition, the EDS results reveal that the atomic ratio of incorporated Co is about 0.71% (Fig. S5†).

To elucidate the changes in elemental composition and chemical state after the electrochemical deposition, XPS analysis was further performed on the (CoNi)O$_x$/Ni(OH)$_2$@NF electrode. As shown in Fig. 3a, the survey spectra of (CoNi)O$_x$/Ni(OH)$_2$@NF clearly display the binding energy peaks of elements Ni, Co, and O, confirming the successful incorporation of Co^{2+} ions onto the surface of NiO$_x$/Ni(OH)$_2$@NF. The binding energy peaks of Ni^{2+} 2p$_{3/2}$ (855.7 eV) and Ni^{2+} 2p$_{1/2}$ (873.3 eV) confirm that Ni–OH bonds remained on the reconstructed surface (Fig. 3b).[34,35] Meanwhile, the binding energy peaks located at 857.0 and 874.9 eV typically belonging to Ni^{3+}

2p$_{3/2}$ and Ni^{3+} 2p$_{1/2}$ reveal the existence of Ni^{3+} species (NiOOH).[36] This indicates that NiOOH remained after the electrochemical deposition process. Fig. 3c shows the high-resolution XPS spectra of Co 2p, where prominent binding energy peaks at 781.0 and 796.8 eV corresponding to Co 2p$_{3/2}$ and Co 2p$_{1/2}$, respectively, confirm the successful incorporation of Co^{2+} ions onto the surface of NiO$_x$/Ni(OH)$_2$@NF.[37–39] The deconvoluted peaks located at 781.9, 797.2, 780.6, and 796.2 eV correspond to Co^{2+} 2p$_{3/2}$, Co^{2+} 2p$_{1/2}$, Co^{3+} 2p$_{3/2}$, and Co^{3+} 2p$_{1/2}$, respectively.[40,41] More importantly, the high-resolution XPS spectra of Co 2p further display two binding energy peaks located at 783.4 and 798.2 eV, which can correspond to Co^{4+} 2p$_{3/2}$ and Co^{4+} 2p$_{1/2}$, respectively. This indicates that highly active Co^{4+} species (CoO$_2$) were prepared on the surface of (CoNi)O$_x$/Ni(OH)$_2$@NF.[42] In addition, the deconvoluted O 1s spectra in Fig. 3d reveal the formation of M–O (530.9 eV) and M–OH (531.5 eV) bonds, corresponding to the derived oxyhydroxides.[41,43] In brief, the XPS results confirm the successful preparation of bimetallic oxy-hydroxides on the surface of (CoNi)O$_x$/Ni(OH)$_2$@NF.

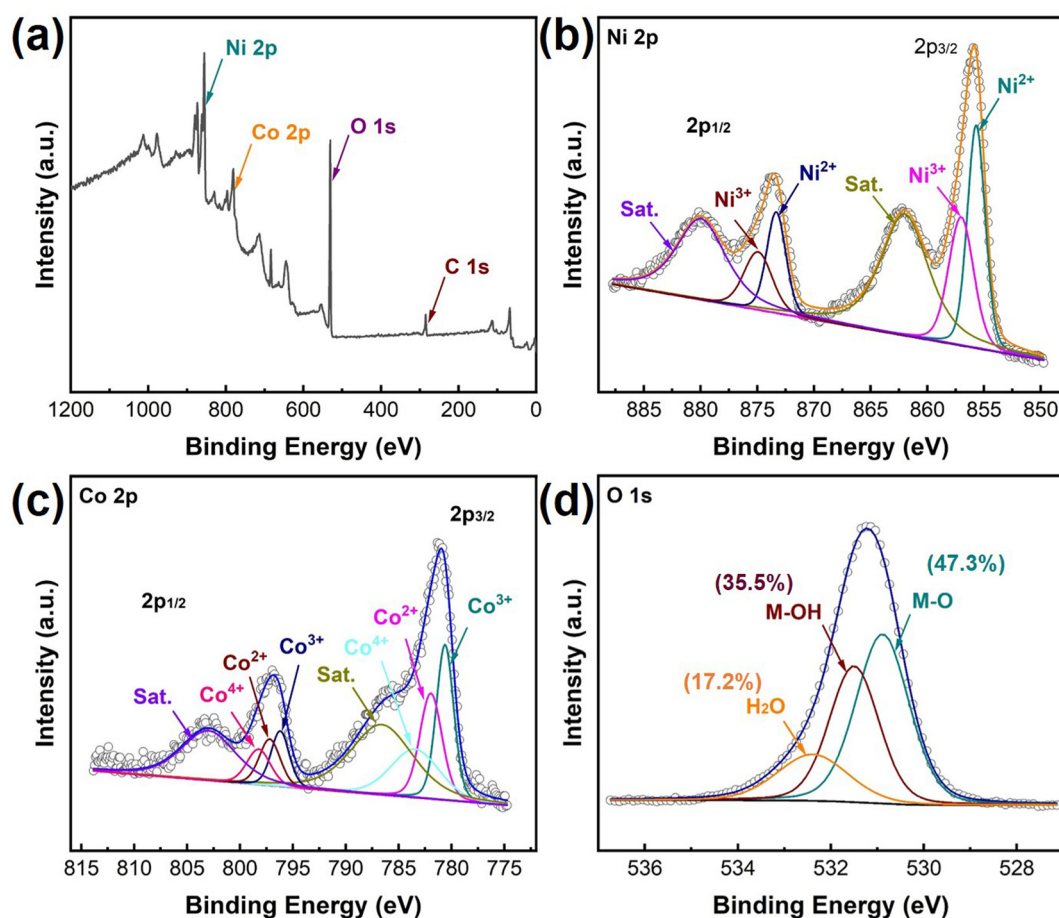To preliminarily investigate the catalytic performance of (CoNi)O$_x$/Ni(OH)$_2$@NF towards glucose oxidation, CV tests were conducted with and without the addition of glucose in
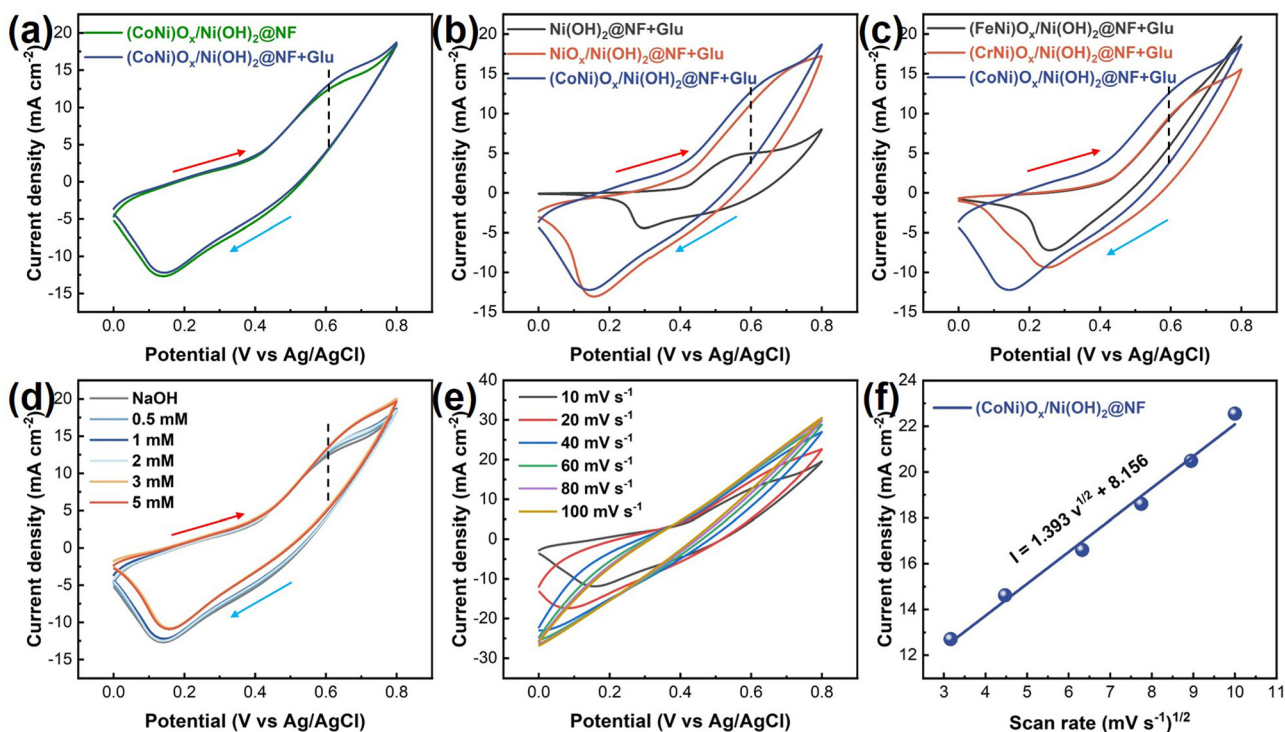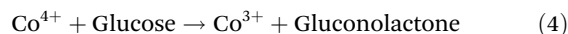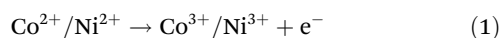

Fig. 3 (a) Survey spectra of (CoNi)O$_x$/Ni(OH)$_2$@NF. High-resolution XPS spectra: (b) Ni 2p, (c) Co 2p, and (d) O 1s.

Fig. 4 (a) CV curves of $(CoNi)O_x/Ni(OH)_2@NF$ at a scan rate of 10 mV s^{-1} with and without the addition of 1 mM glucose. (b) CV curves at a scan rate of 10 mV s^{-1} with the addition of 1 mM glucose. (c) CV curves at a scan rate of 10 mV s^{-1} with addition of 1 mM glucose. (d) CV curves of $(CoNi)O_x/Ni(OH)_2@NF$ with different concentrations of glucose addition. (e) CV curves of $(CoNi)O_x/Ni(OH)_2@NF$ with different scan rates. (f) The current response verses the square root of the scan rate derived from (e).

0.1 M NaOH solution. As shown in Fig. 4a, the CV curve of $(CoNi)O_x/Ni(OH)_2@NF$ exhibits an oxidation peak near 0.58 V (*vs.* Ag/AgCl) and a reduction peak near 0.14 V (*vs.* Ag/AgCl) in the absence of glucose, typically indicating that Co^{2+}/Ni^{2+} are oxidized to Co^{3+}/Ni^{3+} at around 0.58 V (*vs.* Ag/AgCl), and Co^{3+}/Ni^{3+} are reduced back to Co^{2+}/Ni^{2+} at approximately 0.14 V (*vs.* Ag/AgCl).[44] With the addition of 1 mM glucose, the response current was significantly increased with the oxidation peak shifting to around 0.6 V (*vs.* Ag/AgCl) during the CV test. The obviously increased oxidation current density can be ascribed to the oxidation of glucose by the Co/Ni sites of the bimetallic oxy-hydroxides. As reported in the literature, the Ni^{3+} species (NiOOH) were regarded as one of the most active materials for oxidizing glucose to gluconolactone, regardless of the original form of nickel-based materials.[45] Meanwhile, the Co^{4+} species (CoO_2) were also recognized as active materials for glucose sensing.[46] Therefore, based on the valence state changes of Ni^{3+} and Co^{4+} species during glucose oxidation, the following sensing mechanism should be included for $(CoNi)O_x/Ni(OH)_2@NF$:

$$Co^{2+}/Ni^{2+} \rightarrow Co^{3+}/Ni^{3+} + e^- \quad (1)$$

$$Co^{3+} \rightarrow Co^{4+} + e^- \quad (2)$$

$$Ni^{3+} + Glucose \rightarrow Ni^{2+} + Gluconolactone \quad (3)$$

$$Co^{4+} + Glucose \rightarrow Co^{3+} + Gluconolactone \quad (4)$$

More importantly, a new pathway for oxidizing glucose to gluconolactone was proposed based on the reactive-O atoms of $(CoNi)O_x/Ni(OH)_2@NF$, since the reactive-O atoms can contribute to the formation of Ni^{3+} species (NiOOH). With the oxidative Co^{4+} species as electron acceptors, the Ni–O (reactive-O atoms adsorbed on Ni^{2+} sites) can bond with adsorbed OH$^-$ to form Ni–OOH (Ni^{3+} species). The corresponding sensing mechanism was inferred as follows:

$$Co^{4+} + Ni^{2+} + O_{ads} + Glucose \rightarrow Co^{3+} + Ni^{2+}$$
$$+ Gluconolactone \quad (5)$$
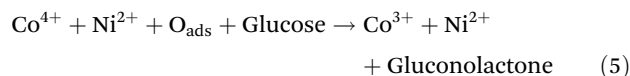
This new pathway can make use of Ni^{2+} sites for oxidizing glucose to gluconolactone with the help of reactive-O atoms and Co^{4+} species, thus enhancing the sensing performance.

CV tests were also performed on $Ni(OH)_2@NF$, $NiO_x/Ni(OH)_2@NF$, $(FeNi)O_x/Ni(OH)_2@NF$, and $(CrNi)O_x/Ni(OH)_2@NF$ electrodes to show the current response for glucose detection. In Fig. S6,† all of the prepared electrodes show ability for glucose detection. However, the $(CoNi)O_x/Ni(OH)_2@NF$ exhibits a current density of 12.8 mA cm^{-2} at the oxidation potential of 0.6 V (*vs.* Ag/AgCl), higher than that of both the $Ni(OH)_2@NF$ (5.0 mA cm^{-2}) and $NiO_x/Ni(OH)_2@NF$ (11.2 mA cm^{-2}) electrodes (Fig. 4b). The significant improvement of $NiO_x/Ni(OH)_2@NF$ compared to $Ni(OH)_2@NF$ can mainly be ascribed to the formation of more Ni^{3+} species due to the

electrochemical oxidation. With the incorporation of Co^{2+} ions as well as the derived Co^{4+} ions, the synergistic effects between the Co/Ni catalytic sites further enhanced the electrocatalytic performance of glucose oxidation. In Fig. S7,† the glucose sensing performance of $Co/Ni(OH)_2@NF$ for which the Co ions were directly deposited on the surface of $Ni(OH)_2@NF$ was evaluated. The response current of $Co/Ni(OH)_2@NF$ with glucose addition is only 4.9 mA cm^{-2}, which is obviously lower than that of $(CoNi)O_x/Ni(OH)_2@NF$. It is worth noting that the ratio of Ni^{3+} species to reactive-O atoms (O_{ads}) for $Ni(OH)_2@NF$ is lower than that of $NiO_x/Ni(OH)_2@NF$ (Fig. S3†). That is to say, without enough Ni^{3+} species and reactive-O atoms, the glucose sensing performance of Co^{4+} species was significantly restricted. Thus, the enhanced glucose sensing performance of $(CoNi)O_x/Ni(OH)_2@NF$ can be ascribed to the synergistic effects between Ni and Co catalytic sites as shown in mechanism (3), (4), and (5). However, mechanism (4) and (5) for the $(FeNi)O_x/Ni(OH)_2@NF$ and $(CrNi)O_x/Ni(OH)_2@NF$ electrodes may be unusable due to the lower activity of Fe_2O_3 and Cr_2O_3. As a result, the response current densities of the $(FeNi)O_x/Ni(OH)_2@NF$ (9.6 mA cm^{-2}) and $(CrNi)O_x/Ni(OH)_2@NF$ (9.8 mA cm^{-2}) electrodes are lower than that of $(CoNi)O_x/Ni(OH)_2@NF$ (Fig. 4c).

Fig. 4d shows the CV curves of $(CoNi)O_x/Ni(OH)_2@NF$ in solutions with varying concentrations of glucose. The current density at the oxidation potential gradually increased with increasing glucose concentration, indicating that $(CoNi)O_x/Ni(OH)_2@NF$ possesses good catalytic ability towards glucose oxidation over a wide concentration range, thus highlighting its potential for constructing glucose sensors.[47] CV tests were also conducted on the $Ni(OH)_2@NF$, $NiO_x/Ni(OH)_2@NF$, $(FeNi)O_x/Ni(OH)_2@NF$, and $(CrNi)O_x/Ni(OH)_2@NF$ electrodes as shown in Fig. S8.† Similarly, all of the prepared electrodes exhibit an enhanced response current on increasing the concentration of glucose in solution, demonstrating the effective electrocatalytic ability of the $Ni(OH)_2@NF$, $NiO_x/Ni(OH)_2@NF$, $(FeNi)O_x/Ni(OH)_2@NF$, and $(CrNi)O_x/Ni(OH)_2@NF$ electrodes towards glucose detection. Fig. 4e presents the CV curves of $(CoNi)O_x/Ni(OH)_2@NF$ in a solution containing 0.1 M NaOH and 1 mM glucose, recorded at different scan rates ranging from 10 to 100 mV s^{-1}. As shown in Fig. 4f, the corresponding oxidation current density improved with increasing scan rate, showing a linear relationship with the square root of the scan rate, and revealing a diffusion-controlled electrochemical process.[48] The CV curves of the other four electrodes at different scan rates are shown in Fig. S9,† similarly demonstrating the corresponding linear relationships (Fig. S10†).

To determine the optimal potential of $(CoNi)O_x/Ni(OH)_2@NF$ for glucose detection, chronoamperometry tests with incremental addition of 1 mM glucose were applied at potentials ranging from 0.4 to 0.65 V (vs. Ag/AgCl). As shown in Fig. 5a, the $(CoNi)O_x/Ni(OH)_2@NF$ electrode exhibits an obvious current response to glucose across all the chosen voltages applied. The corresponding ΔI increased with higher voltages applied, reaching the maximum value at 0.6 V (vs. Ag/

AgCl) and decreasing at 0.65 V (vs. Ag/AgCl). In Fig. 5b, the corresponding concentration-current fitting lines of different applied voltages display that the largest slope appeared at 0.6 V (vs. Ag/AgCl). In this regard, the optimal potential of $(CoNi)O_x/Ni(OH)_2@NF$ for glucose detection is determined to be 0.6 V (vs. Ag/AgCl), and thus the voltage of 0.6 V (vs. Ag/AgCl) was selected as the working voltage for $(CoNi)O_x/Ni(OH)_2@NF$ in subsequent measurements. With the same testing method, the optimal potentials for the $Ni(OH)_2@NF$, $NiO_x/Ni(OH)_2@NF$, $(FeNi)O_x/Ni(OH)_2@NF$, and $(CrNi)O_x/Ni(OH)_2@NF$ electrodes were determined to be 0.6, 0.6, 0.5, and 0.6 V (vs. Ag/AgCl), respectively (Fig. S11†).

The detailed glucose sensing performance of $(CoNi)O_x/Ni(OH)_2@NF$ was obtained through a chronoamperometry test by sequentially adding glucose at 50 s intervals. The amount of glucose addition changed every 150 s, and these changes were marked with downward pointing arrows and the corresponding amounts of glucose on the i–t curve. As the i–t curve in Fig. 5c shows, the current density quickly rises to a steady state with the addition of glucose, demonstrating its efficient glucose sensing capability. A noticeable current response is observed starting from the glucose concentration of 10 μM, indicating sensitive detection at low concentrations. Furthermore, the response current continuously improves with increasing concentration of glucose until 11.04 mM. The linear fitting between glucose concentration and response current is depicted in Fig. 5d, showing a significant linear relationship within the range of 10 μM to 1.14 mM. The linear fitting equation is $I(mA) = 3.5903C(mM) + 2.133$, with an R^2 value of 0.9969, yielding a sensitivity of 3590.3 μA mM^{-1} cm^{-2}. Additionally, i–t curves with varying glucose concentrations were recorded for the $Ni(OH)_2@NF$, $NiO_x/Ni(OH)_2@NF$, $(FeNi)O_x/Ni(OH)_2@NF$, and $(CrNi)O_x/Ni(OH)_2@NF$ electrodes as shown in Fig. S12.† According to the linear fitting results in Fig. S13,† the corresponding sensitivity values for $Ni(OH)_2@NF$, $NiO_x/Ni(OH)_2@NF$, $(FeNi)O_x/Ni(OH)_2@NF$, and $(CrNi)O_x/Ni(OH)_2@NF$ within their respective response ranges are reported as 698.3, 1504.0, 637.7, and 2810.6 μA mM^{-1} cm^{-2}, respectively (Fig. 5e). Furthermore, the sensitivity of $(CoNi)O_x/Ni(OH)_2@NF$ is competitive with the recently reported non-enzymatic electrocatalysts as shown in Table S1.† This highlights that $(CoNi)O_x/Ni(OH)_2@NF$ exhibits outstanding sensitivity, making it advantageous for catalyzing glucose oxidation. Apart from the sensitivity, the response time is also crucial in evaluating the glucose sensing performance. Fig. 5f demonstrates that $(CoNi)O_x/Ni(OH)_2@NF$ achieves a rapid response within 4 s upon adding 1 mM glucose to the electrolyte, indicating its potential for real-time glucose concentration detection. The i–t curves to determine the response times of the $Ni(OH)_2@NF$ (4 s), $NiO_x/Ni(OH)_2@NF$ (4 s), $(FeNi)O_x/Ni(OH)_2@NF$ (6 s), and $(CrNi)O_x/Ni(OH)_2@NF$ (10 s) electrodes are shown in Fig. S14.† As a result, the $(CoNi)O_x/Ni(OH)_2@NF$ exhibits a lower response time, showing a rapid response for glucose sensing (Fig. 5g).

Considering that for practical applications glucose sensors must exhibit specificity in detecting target analytes among
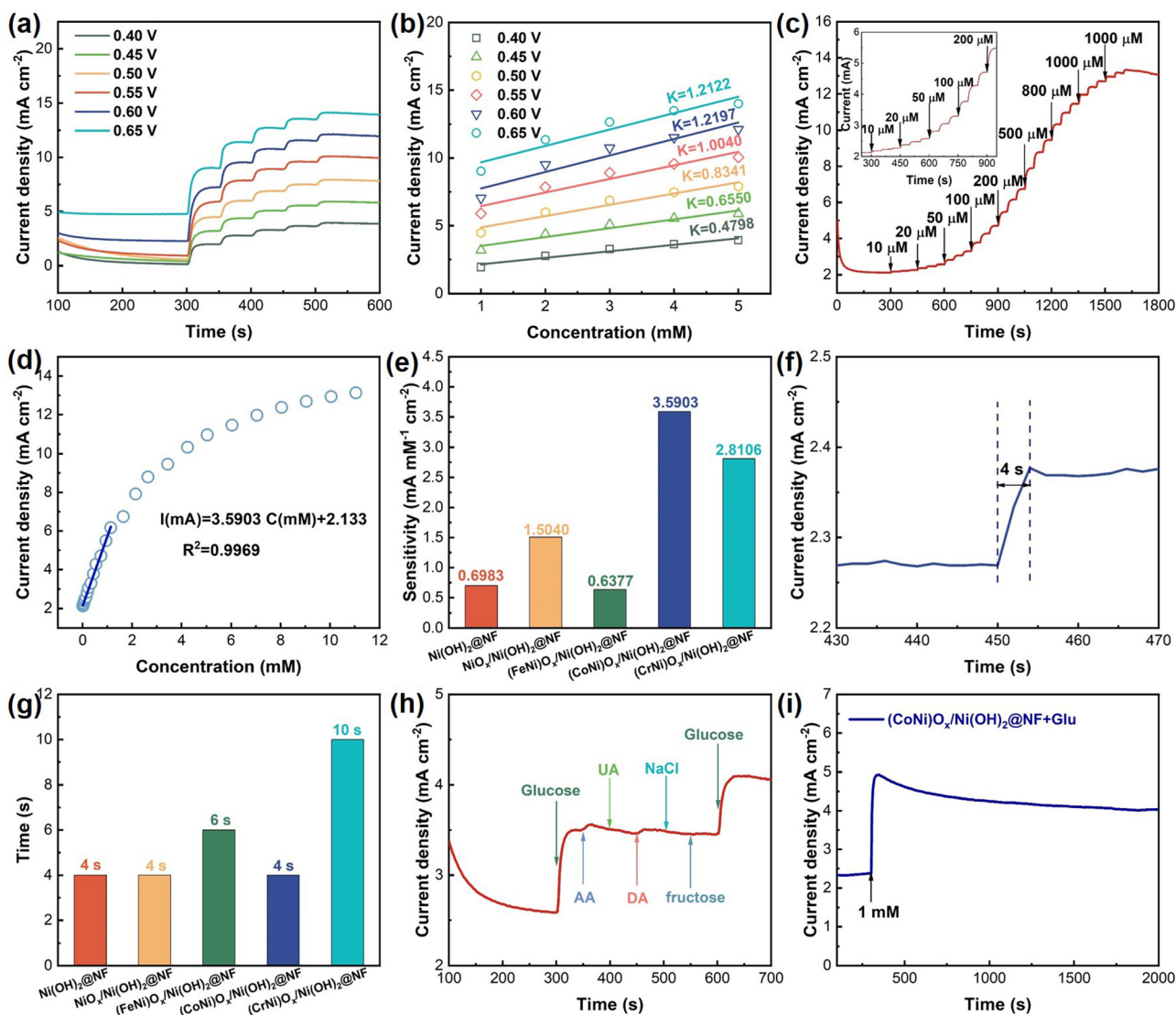
Fig. 5 (a) $i-t$ curves of $(CoNi)O_x/Ni(OH)_2@NF$ at different voltages with incremental addition of 1 mM glucose. (b) The corresponding concentration–current fitting curves of (a). (c) $i-t$ curve of $(CoNi)O_x/Ni(OH)_2@NF$ at a potential of 0.6 V (*vs.* Ag/AgCl) with addition of different concentrations of glucose. (d) The corresponding concentration–current fitting curve of (c). (e) The sensitivity of the prepared samples. (f) $i-t$ curve of $(CoNi)O_x/Ni(OH)_2@NF$ with the addition of 10 μM glucose. (g) The current response time of the prepared samples. (h) $i-t$ curve of $(CoNi)O_x/Ni(OH)_2@NF$ with the addition of glucose, AA, UA, DA, NaCl, and fructose. (i) Long-term stability of $(CoNi)O_x/Ni(OH)_2@NF$ with the addition of 1 mM glucose.

various interfering substances commonly found in serum, the anti-interference performance was investigated through a chronoamperometry test by adding AA, UA, DA, NaCl, and fructose. Fig. 5h illustrates that the $(CoNi)O_x/Ni(OH)_2@NF$ electrode displays no significant fluctuations when adding AA, UA, DA, NaCl, and fructose into the electrolyte. However, it still maintains a sensitive response to glucose even after sequential addition of these potential interferents, demonstrating its robust anti-interference capability. Comparable results are observed for the $Ni(OH)_2@NF$, $NiO_x/Ni(OH)_2@NF$, $(FeNi)O_x/Ni(OH)_2@NF$, and $(CrNi)O_x/Ni(OH)_2@NF$ electrodes as shown in Fig. S15.† Stability is essential for prolonged sensor application. Fig. 5i shows that $(CoNi)O_x/Ni(OH)_2@NF$

keeps a high current response in a 2000 s test period, indicating its excellent electrochemical stability suitable for long-term testing. Stability tests for the $Ni(OH)_2@NF$, $NiO_x/Ni(OH)_2@NF$, $(FeNi)O_x/Ni(OH)_2@NF$, and $(CrNi)O_x/Ni(OH)_2@NF$ electrodes are depicted in Fig. S16,† showing satisfactory electrochemical stability. Overall, the $(CoNi)O_x/Ni(OH)_2@NF$ electrode exhibits superior performance in terms of sensitivity, immunity to interference, and stability, making it highly promising for sensitive glucose detection applications. This suggests that $(CoNi)O_x/Ni(OH)_2@NF$, synthesized *via* the electrochemical oxidation of $Ni(OH)_2$ nanosheets, and incorporated with Co^{2+} ions, represents a feasible approach for high-performance non-enzyme glucose sensors.

4. Conclusion

In conclusion, this study successfully prepared bimetallic oxy-hydroxides based on $Ni(OH)_2$ nanosheets ($(CoNi)O_x$/$Ni(OH)_2$@NF) as a high performance sensing material for glucose detection. The sheet-like morphology of the $Ni(OH)_2$ template is helpful for improving the specific surface area of the electrode. The electrochemical oxidation of $Ni(OH)_2$@NF creates an active surface with abundant Ni^{3+} species and reactive-O atoms formed. In addition, Co^{2+} ions are incorporated onto the active surface and Co^{4+} species are derived due to the electrochemical deposition. A new pathway for oxidizing glucose to gluconolactone is proposed based on Ni^{2+} sites, reactive-O atoms and Co^{4+} species for the $(CoNi)O_x$/$Ni(OH)_2$@NF. The synergistic effects of the Co/Ni active sites contribute to the enhanced catalytic activity of $(CoNi)O_x$/$Ni(OH)_2$@NF for glucose sensing. The optimized $(CoNi)O_x$/$Ni(OH)_2$@NF exhibits a high sensitivity of 3590.3 μA mM^{-1} cm^{-2} in a linear range of 10 μM to 1.14 mM, and a fast response time of less than 4 s. Furthermore, the $(CoNi)O_x$/$Ni(OH)_2$@NF also demonstrated good anti-interference properties and long-term stability. These findings suggest that $(CoNi)O_x$/$Ni(OH)_2$@NF is a promising non-enzymatic glucose sensing material.

Data availability

All relevant data are within the paper and its additional files.

Conflicts of interest

The authors declare no competing financial interest.

Acknowledgements

References

1 L. Heinemann, G. Freckmann, D. Ehrmann, G. Faber-Heinemann, S. Guerra, D. Waldenmaier and N. Hermanns, *Lancet*, 2018, **391**, 1367–1377.

2 J. C. Pickup, S. C. Freeman and A. J. Sutton, *Br. Med. J.*, 2011, **343**, 1–14.

3 J. B. Buse, D. J. Wexler, A. Tsapas, P. Rossing, G. Mingrone, C. Mathieu, D. A. D'Alessio and M. J. Davies, *Diabetologia*, 2020, **63**, 221–228.

4 Y. Liu, H. Teng, H. Hou and T. You, *Biosens. Bioelectron.*, 2009, **24**, 3329–3334.

5 X. Sun and F. Xiao, *J. Food Meas. Charact.*, 2024, **18**, 9465–9472.

6 A. Le Goff, M. Holzinger and S. Cosnier, *Analyst*, 2011, **136**, 1279–1287.

7 M. H. Hassan, C. Vyas, B. Grieve and P. Bartolo, *Sensors*, 2021, **21**, 4672.

8 F. Franceschini and I. Taurino, *Phys. Med.*, 2022, **14**, 100054.

9 J. Morshed, R. Nakagawa, M. M. Hossain, Y. Nishina and S. Tsujimura, *Biosens. Bioelectron.*, 2021, **189**, 113357.

10 S. Cinti, R. Marrone, V. Mazzaracchio, D. Moscone and F. Arduini, *Biosens. Bioelectron.*, 2020, **165**, 112334.

11 Y. Wang, Y. Wang, L. Y. S. Lee and K. Y. Wong, *Nanoscale*, 2023, **15**, 18173–18183.

12 D. E. Pissinis, L. E. Sereno and J. M. Marioli, *Sens. Actuators, B*, 2014, **193**, 46–52.

13 Y. Chen, P. Wang, H. Hao, J. Hong, H. Li, S. Ji, A. Li, R. Gao, J. Dong, X. Han, M. Liang, D. Wang and Y. Li, *J. Am. Chem. Soc.*, 2021, **143**, 18643–18651.

14 Y. Xu, X. Zhang, X. S. Zhu and Y. W. Shi, *Nanoscale*, 2024, **16**, 7085–7092.

15 M. Smiljanić, S. Panić, M. Bele, F. Ruiz-Zepeda, L. Pavko, L. Gašparič, A. Kokalj, M. Gaberšček and N. Hodnik, *ACS Catal.*, 2022, **12**, 13021–13033.

16 B. E. Conway and B. V. Tilak, *Electrochim. Acta*, 2002, **47**, 3571–3594.

17 G. Chang, H. Shu, Q. Huang, M. Oyama, K. Ji, X. Liu and Y. He, *Electrochim. Acta*, 2015, **157**, 149–157.

18 S. Nantaphol, T. Watanabe, N. Nomura, W. Siangproh, O. Chailapakul and Y. Einaga, *Biosens. Bioelectron.*, 2017, **98**, 76–82.

19 W. Zhao, R. Zhang, S. Xu, J. Cai, X. Zhu, Y. Zhu, W. Wei, X. Liu and J. Luo, *Biosens. Bioelectron.*, 2018, **100**, 497–503.

20 S. Song, X. Ma, W. Li, B. Zhang, B. Shao, X. Chang and X. Liu, *J. Alloys Compd.*, 2023, **931**, 167413.

21 H. Ai, X. Huang, Z. Zhu, J. Liu, Q. Chi, Y. Li, Z. Li and X. Ji, *Biosens. Bioelectron.*, 2008, **24**, 1048–1052.

22 R. Li, X. Liu, H. Wang, Y. Wu, K. C. Chan and Z. Lu, *Electrochim. Acta*, 2019, **299**, 470–478.

23 H. Y. Li, A. K. Lu and S. S. Wang, *J. Alloys Compd.*, 2022, **921**, 165995.

24 Z. Shao, Q. Gao, S. Sun, L. Wu and W. Feng, *Sens. Actuators, B*, 2024, **398**, 134713.

25 B. Zhan, C. Liu, H. Chen, H. Shi, L. Wang, P. Chen, W. Huang and X. Dong, *Nanoscale*, 2014, **6**, 7424–7429.

26 H. Nie, Z. Yao, X. Zhou, Z. Yang and S. Huang, *Biosens. Bioelectron.*, 2011, **30**, 28–34.

27 K. Tian, M. Prestgard and A. Tiwari, *Mater. Sci. Eng., C*, 2014, **41**, 100–118.

28 X. Yang, P. Jiao, G. Zhu, Y. Zeng, Q. Wang, G. Qiu, C. Wang and H. Yu, *Colloids Surf., A*, 2024, **703**, 135301.

29 X. Di, Y. Pan, W. Dai, Y. an Zhu and T. Lu, *Mater. Lett.*, 2020, **271**, 127694.

30 Q. Du, Y. Liao, N. Shi, S. Sun, X. Liao, G. Yin, Z. Huang, X. Pu and J. Wang, *J. Electroanal. Chem.*, 2022, **904**, 115887.

31 A. Vignesh, P. Vajeeston, M. Pannipara, A. G. Al-Sehemi, Y. Xia and G. G. Kumar, *Chem. Eng. J.*, 2022, **430**, 133157.

32 B. Wu, W. Dai, X. Yang, C. Zhao, Y. Zhang, C. Cui, Y. Sui, P. Cao and S. Huang, *Fuel*, 2024, **374**, 132450.

33 Y. Ding, B. Q. Miao, Y. Zhao, F. M. Li, Y. C. Jiang, S. N. Li and Y. Chen, *Chin. J. Catal.*, 2021, **42**, 271–278.

34 H. Y. Zhao, R. Y. Fan, Z. Y. Zhao, X. Y. Zhang, B. Dong, Q. X. Lv, X. Liu, B. Liu and Y. M. Chai, *Fuel*, 2023, **332**, 125780.

35 X. H. Wang, R. Yuan, S. Bin Yin, Q. L. Hong, Q. G. Zhai, Y. C. Jiang, Y. Chen and S. N. Li, *Adv. Funct. Mater.*, 2024, **34**, 1–10.

36 J. Kim, J. E. Yoo and K. Lee, *Energy Environ. Mater.*, 2024, 1–7.

37 S. Bai, W. Dai, X. Yang, B. Wu, J. Guo, C. Zhao, Y. Zhang, C. Cui, G. Zou and S. Huang, *Int. J. Hydrogen Energy*, 2024, **84**, 615–622.

38 Q. L. Hong, Q. G. Zhai, X. L. Liang, Y. Yang, F. M. Li, Y. C. Jiang, M. C. Hu, S. N. Li and Y. Chen, *J. Mater. Chem. A*, 2021, **9**, 3297–3302.

39 J. Miao, Q. Hong, L. Liang, G. Li, Z. Liu, S. Yin and Y. Chen, *Chin. Chem. Lett.*, 2024, **35**, 108935.

40 T. Hou, R. Yang, J. Xu, X. He, H. Yang, P. W. Menezes and Z. Chen, *Nanoscale*, 2024, **16**, 15629–15639.

41 Y. Ma, Y. Ha, L. Chen, Z. An, L. Xing, Z. Wang and Z. Li, *Small*, 2024, **20**, 1–12.

42 Y. K. Huang, T. Li, H. Feng, L. T. Lv, T. X. Tang, Z. Lin, K. H. Ye and Y. Q. Wang, *Small*, 2024, **2407443**, 1–11.

43 Y. Zhou, J. Zeng, X. Zheng, W. Huang, Y. Dong, J. Zhang, Y. Deng and R. Wu, *J. Colloid Interface Sci.*, 2025, **678**, 536–546.

44 M. Wei, Y. Qiao, H. Zhao, J. Liang, T. Li, Y. Luo, S. Lu, X. Shi, W. Lu and X. Sun, *Chem. Commun.*, 2020, **56**, 14553–14569.

45 X. Y. Wang, X. X. Yan, Y. P. Wu, X. Q. Wu, Y. M. Yin, S. Li, Q. Zhang, B. Liu and D. S. Li, *Inorg. Chem.*, 2023, **62**, 10256–10262.

46 Y. Liu, X. Cao, R. Kong, G. Du, A. M. Asiri, Q. Lu and X. Sun, *J. Mater. Chem. B*, 2017, **5**, 1901–1904.

47 W. Cao, T. Guo, Y. Ding, Y. Hu and D. Liu, *Appl. Surf. Sci.*, 2023, **634**, 157650.

48 X. Li, J. Yao, F. Liu, H. He, M. Zhou, N. Mao, P. Xiao and Y. Zhang, *Sens. Actuators, B*, 2013, **181**, 501–508.